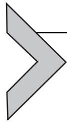

CHAPTER THREE

Compound Semiconductor Nanowire Photodetectors

Xing Dai*, Maria Tchernycheva*, Cesare Soci†,1
*Institut d'Electronique Fondamentale, UMR 8622 CNRS, University Paris Sud XI, Orsay Cedex, France
†School of Physical and Mathematical Sciences, School of Electrical and Electronic Engineering, and Centre for Disruptive Photonic Technologies, Nanyang Technological University, Singapore, Singapore
[1]Corresponding author: e-mail address: csoci@ntu.edu.sg

Contents

1. Introduction 75
2. Nanowire Photoconductors 77
   2.1 General Description of Nanowire Photoconductivity 77
   2.2 Light Absorption 80
   2.3 Nanowire Photoconductor Materials 82
3. Phototransistors 88
4. Nanowire Heterostructures 90
   4.1 Homogeneous and Heterogeneous Photodiode Junctions 90
   4.2 Schottky Junctions 94
   4.3 Avalanche Photodiodes 98
5. Summary and Conclusions 99
Acknowledgments 100
References 101

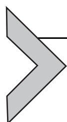

1. INTRODUCTION

Light detection by semiconductor nanowires (NWs) is an active area of research. The interest in NW photodetector devices was originally motivated by the fascinating properties of NW materials and structures, which offer new ways to improve the detector performance as well as to integrate multiple functionalities. Indeed, NWs exhibit unique photonic and electrical properties stemming from their anisotropic geometry, high surface-to-volume ratio, small footprint, and crystalline perfection. Even above the quantum confinement size regime, NW photoconductors can yield higher light sensitivity than their bulk counterparts due to the large

Semiconductors and Semimetals, Volume 94
ISSN 0080-8784
http://dx.doi.org/10.1016/bs.semsem.2015.08.001
© 2016 Elsevier Inc.
All rights reserved.

surface-to-volume ratio and small dimensions. The waveguiding properties of individual NWs as well as the antireflection and light trapping properties of NW arrays are also beneficial for light detection since efficient absorption can be achieved within a small volume of active material. Availability of compound semiconductor materials and functional NW heterostructures, either axial or radial, has enabled bandgap engineering and translation of conventional photodetector device concepts into NW architectures. In addition, NWs can be integrated with CMOS technology either by direct growth of high-quality nanocrystals on Si or by different transfer schemes such as dielectrophoresis or dry printing. Integration of NW detectors and light emitters into functional platforms for optical interconnects, quantum photonics and biosensors is currently an area of intense activity and growing interest in both electronics and photonics research communities.

Thanks to the ongoing advancement in the growth and fabrication methodologies, NWs of almost all the existing semiconductor materials can be now realized by means of either top-down or bottom-up approaches. The advantage of the bottom-up NW synthesis is the possibility to reduce the object dimensions disregarding the limitations imposed by the lithographic techniques while preserving lateral surface flatness. A high degree of control over the composition, doping, and morphology is achieved today with a bottom-up approach. It has also become possible to integrate different functionalities in NWs, using doping and homo- or heterojunctions of compound semiconductor materials, in order to engineer their properties at the nanoscale.

The fabrication of NW photodetectors can follow different designs. The most popular are the in-plane architecture, with the electro-optically active NWs lying on a substrate and the vertical architecture, with the NWs standing generally on their native growth substrate. The in-plane geometry can be applied to both single wire and array detectors. In this design, the wires are either randomly dispersed or prepositioned using some alignment techniques (e.g., dielectrophoresis, contact printing, etc.) and contacted by lithographic techniques. The vertical configuration has been mainly reserved to the demonstration of NW array devices using a large number of parallel-connected NWs as an active medium. These different photodetector designs will be discussed in the following sections providing examples of specific realizations.

This chapter is organized as follows: in Section 2, we will introduce the basic concepts of photoconductivity and photoconductive gain in NW photoconductors, highlighting some of the unique optical and photoconductive properties of NWs and NW arrays. We will also review some of

the reports on photosensitivity in compound semiconductor NW photoconductors, grouped by material categories; in Section 3, we will discuss NW phototransistors, where photosensitivity is greatly enhanced by an additional gate bias; in Section 4, we will deal with some heterostructure NW device concepts demonstrated in the literature, including homo-/heterojunction and Schottky photodiodes. Practical examples from recent experimental work will be given in each of these sections. Finally, in Section 4, we will summarize and provide an overview on perspective development of the field.

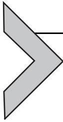

2. NANOWIRE PHOTOCONDUCTORS

Photoconductivity is a well-known property of semiconductors that change their electrical conductivity under illumination (Bube, 1960). Photoconductive semiconductors have broad application in light detection and photovoltaic energy conversion. The observation of high photoresponsivity in semiconductor NWs and recent advances in the understanding of the photoconduction mechanism in low-dimensional systems with a high density of surface states is attracting growing interest for the potential use of NWs as photosensing elements in highly integrated optoelectronic devices, optical interconnects, transceivers, etc. The basic concepts specifically related to photoconductivity in NWs are presented in the following.

2.1 General Description of Nanowire Photoconductivity

The intrinsic conductivity $[\sigma]=[\mathrm{A\ V^{-1}\ cm^{-1}}]$ of a semiconductor in the dark is given by:

$$\sigma = en\mu \tag{1}$$

where e the electronic charge, n is the charge carrier density (for simplicity, only one type of carriers is considered) and μ is the carrier mobility $[\mu]=[\mathrm{cm^2\ V^{-1}\ s^{-1}}]$. In the presence of an applied electric field $F=V/l$ (V being the voltage applied across a NW with length l), the current is given by:

$$I = \sigma FS = envS \tag{2}$$

where $v=\mu F$ is the carrier drift velocity and S is the nondepleted cross-section surface of the NW. Due to the pinning of the Fermi energy at the NW lateral surface, NWs exhibit a depletion space-charge layer and

the conducting surface S is in general smaller than the physical NW cross section. Band bending at the surface provides physical separation of electrons and holes and can lead to a significantly enhanced photocarrier lifetime (persistent photoconductivity). A schematic of surface state effects on band bending and photogenerated carrier separation in n-type NWs with different diameters is depicted in Fig. 1.

Under illumination, a change in conductivity $\Delta\sigma$ (photoconductivity) might occur either due to a change in the carrier concentration Δn (carrier photogeneration) or to a change in the carrier mobility $\Delta\mu$:

$$\Delta\sigma = \sigma_{\text{light}} - \sigma_{\text{dark}} = e(\mu\Delta n + n\Delta\mu) \tag{3}$$

For bulk photoconductors, the conducting surface S is usually considered as constant. However, in the NW case, the conducting surface can be modified. Indeed, the width of the depletion region at the NW surface can be changed under illumination. In general:

$$I_{\text{PC}}(t) = [\mu(t)S\Delta n(t) + n(t)S\Delta\mu(t) + n(t)\mu(t)\Delta S]eF \tag{4}$$

where I_{PC} is the photocurrent. In many semiconductors $\Delta n \gg \Delta\mu$ and the time dependence of the mobility is negligible, therefore the second $[n(t)S\Delta\mu(t)]$ term can be neglected. The third $[n(t)\mu(t)\Delta S]$ term depends on the NW doping and dimensions and can be quite large. The expression for the photocurrent is thus given by:

$$I_{\text{PC}}(t) = e\mu(\Delta n(t)S + n(t)\Delta S)F \tag{5}$$

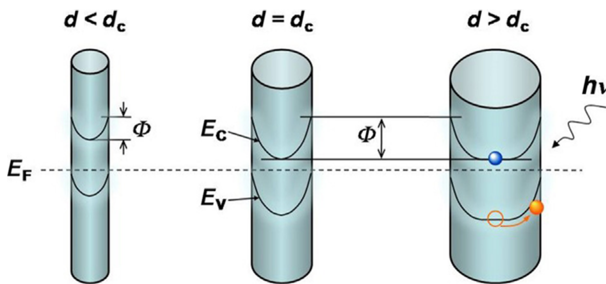

Figure 1 Schematic of the dependence of valence (E_V) and conduction (E_C) band profiles in NWs with different diameters d. Below the critical diameter d_c, the NW is fully depleted and band bending is minimal. For larger diameters, the recombination barrier Φ increases, thus the photocarrier lifetime is prolonged. The detail on the right shows the charge carrier separation mechanism upon photoexcitation. *Adapted from Soci et al. (2010).*

Let us consider a cylindrical NW, with diameter d and length l, of a volume $\mathrm{Vol} = \pi l d^2/4$. The average optical generation rate over the thickness of the NW would then be:

$$g_{\mathrm{d}} = \eta^* \left(P_{\mathrm{opt}}/\hbar\omega\right)/\mathrm{Vol} = 4\eta^* \left(P_{\mathrm{opt}}/\hbar\omega\right)/\pi l d^2 = 4\left(P_{\mathrm{abs}}/\hbar\omega\right)/\pi l d^2 \quad (6)$$

where P_{opt} is the incident optical power on the NW projected surface area, ω is the optical frequency, $\eta^* = \eta\eta^\dagger$ is the effective carrier photogeneration quantum efficiency ($\eta^\dagger$ accounts for the effects of light reflection, light scattering and low dimensionality on the NW absorption, and η is the quantum efficiency), and $P_{\mathrm{abs}} = \eta^* P_{\mathrm{opt}}$ is the absorbed power. Photoexcited carriers relax to the ground state with a characteristic lifetime τ. Therefore, at steady-state under constant illumination, the density of photogenerated carriers will be:

$$\Delta n(t) = g_{\mathrm{d}}\tau = \mathrm{const.} \quad (7)$$

By combining Eqs. (5)–(7), the total steady-state photocurrent in the NW, for a given photon energy, can be written as:

$$I_{\mathrm{PC}} = eF\mu \left[\frac{4}{\pi l d^2}\left(P_{\mathrm{abs}}/\hbar\omega\right)\tau S + n\Delta S\right] \quad (8)$$

The photoconductive gain of the detector defined as a number of detected carriers per absorbed photon can be expressed as

$$G = \frac{N_{\mathrm{e}}}{N_{\mathrm{ph}}} = \frac{I_{\mathrm{PC}}/e}{P_{\mathrm{abs}}/\hbar\omega} \quad (9)$$

We define the carrier transit time $\tau_t = \frac{l}{v} = \frac{l}{\mu F}$, where v is the electron velocity. Then the expression for the photoconductive gain takes the form

$$G = \frac{\tau}{\tau_t}\frac{S}{\pi d^2/4} + \frac{F\mu n\Delta S}{P_{\mathrm{abs}}/\hbar\omega} \quad (10)$$

The first term is the usual expression for the gain, which is the ratio of carrier lifetime to carrier transit time, modified by the ratio between the conducting surface and the total NW cross section. It can be understood as a number of times the photogenerated carrier goes around the electrical circuit before recombination. The second term in (10) reflects the modulation of the conducting cross section due to the hole trapping at the lateral surface similar to the model described by Garrido et al. for GaN 2D layers (Garrido et al., 1998). For the specific NW geometry with a very high

surface-to-volume ratio, this term can be much stronger than in the 2D case. The estimation of the variation of the conducting surface ΔS due to the modulation of the depletion region can be found in Zhang et al. (2013).

Overall, semiconductor NWs show high photoconductive gain due to a combination of the following: (1) the photocarrier lifetime is considerably prolonged due to charge separation promoted by surface states, (2) the carrier transit time is significantly reduced due to the high mobility achievable in high-quality, defect-free single crystal NWs combined with small interelectrode distances, and (3) the conducting surface changes due to the modulation of the depletion region. Numerous experimental studies of the NW photoconductivity have indeed reported a high sensitivity to light and a very high photoconductive gain (Calarco et al., 2005; Jie et al., 2006; Prades et al., 2008a; Reui-San et al., 2007; Soci et al., 2007).

2.2 Light Absorption

Light absorption in NW materials is subject to specific effects stemming from the NW geometry and the low dimensionality, such as optical birefringence, light scattering, and waveguiding effects (light funneling), which will now be discussed in more detail.

2.2.1 Optical Birefringence and Light Polarization Effects

In general, the absorption properties of semiconducting NWs are strongly dependent on the polarization of the incident radiation (Ruda and Shik, 2005, 2006; Wilhelm et al., 2012). The direct observation of such effects on the optical function is quite challenging (Qi et al., 2003; Zhang et al., 2006a). Nevertheless, these effects are easily manifested in photoconductivity and photoluminescence measurements. The two major mechanisms responsible for this phenomenon are: (1) the modification of energy spectrum and optical matrix elements by size quantization of carriers (Peter and Kerry, 1990; Xinyuan et al., 2004) and (2) the dielectric confinement of the optical electric field due to the difference in the dielectric constants of the NW ε and the environment ε_0 (Ruda and Shik, 2005, 2006). While the first mechanism is significant only in very thin NWs ($a < 10$ nm, where a is the NW diameter), the relevance of the latter is dictated exclusively by the ratio of $\varepsilon/\varepsilon_0$ (typically $\varepsilon/\varepsilon_0 > 10$), although it has to be treated differently whether the light wavelength exceeds the NW diameter or not. In the case of thin NWs ($a < \lambda$, i.e., $a < 100$ nm) it has been shown that the ratio of the absorption coefficient for light polarization parallel and perpendicular to the NW axis is given by Ruda and Shik (2005):

$$\frac{k_{\parallel}}{k_{\perp}} = \left| \frac{\varepsilon + \varepsilon_0}{2\varepsilon_0} \right|^2 \tag{11}$$

due to the suppression of the perpendicular component of the electric field vector inside the wire. The factor in Eq. (11) exceeds 30 for most semiconductor NWs. For thicker NWs (or at higher light frequencies), $a > \lambda$, the nonuniform distribution of the field inside the wire must also be taken into account and the ratio of $k_{\parallel}/k_{\perp}$ becomes strongly dependent upon frequency. At certain critical points, the electric field modes are purely transverse, leading to oscillations of $k_{\parallel}/k_{\perp}$ from positive to negative (Ruda and Shik, 2006).

Light polarization dependence of the photoconductivity has been experimentally observed in single NWs of a variety of material systems, including InP (Wang et al., 2001), ZnO (Fan et al., 2004), GaN (Gonzalez-Posada et al., 2012; Han et al., 2004), p-Si/n-CdS and p-i-n-Si nano-avalanche photodiodes (Hayden et al., 2006; Yang et al., 2006), and InAs/InAsP axial heterojunction infrared photodetectors (Pettersson et al., 2006). Anisotropy of the optical absorption results in photocurrent amplitudes varying as:

$$I_{\mathrm{PC}} = I_{\mathrm{PC}}^{0} \cos^2\vartheta \tag{12}$$

where ϑ is the light polarization angle with respect to the principal NW axis. Strong dependence of optical absorption on light polarization is therefore to be expected also in ordered NW arrays, where NWs can be aligned either horizontally or vertically with respect to the substrate.

2.2.2 Light Scattering and Absorption Enhancement in Vertical NW Arrays

Enhanced light scattering is expected in NW structures, when the physical dimensions become comparable to or significantly smaller than the wavelength of the incident radiation. The light trapping in NW ensembles has been extensively studied theoretically showing the possibility to achieve efficient absorption with a small amount of active material, which present a great advantage for photovoltaic applications (Garnett and Yang, 2010). Because of the intrinsic anisotropy of NWs, enhanced light scattering can lead to interesting phenomena such as giant optical birefringence (Muskens et al., 2006) or optical funneling (Hu and Chen, 2007). Effective-medium models predict a significant reduction of the reflectance of vertical NW arrays over the entire spectral range, due to the low effective refractive index of the array of NWs surrounded by air (the NW array acts as a stepped-index antireflection coating; Hu and Chen, 2007;

Muskens et al., 2008). However, for closely packed NW structures, the electromagnetic interaction between NWs cannot be neglected when evaluating their optical properties. Numeric calculations have shown that Si NW arrays approach total absorption of incident light at small wavelengths (Hu and Chen, 2007), due to the confinement of the electromagnetic energy into the high refractive index NW volume (light funneling), thus outperforming their thin-film counterparts.

The optical properties of vertical arrays of InP, Si, GaAs, and GaP NWs have been investigated experimentally (Muskens et al., 2008). It was found that, for typical NW diameters around 50 nm, diffuse multiple light scattering dominates the optical properties of the NW arrays and that depending on the ratio between the absorption and scattering mean free path (the latter can be controlled by varying the NW diameter or by infiltration with refractive index matching materials), absorption losses can be strongly suppressed in the NW arrays. This has obvious implications for the design of efficient NW absorbers in NW-based photovoltaic cells, or in determining the spectral response of NW photodetectors.

2.3 Nanowire Photoconductor Materials

NW photoconductors are the simplest configuration of NW-based photodetectors. In this section, we briefly review the properties of NW photoconductors based on material categories. For ease of comparison, basic parameters of compound semiconductors are summarized in Table 1.

2.3.1 Group III–V Compounds

III–V compound semiconductors are among the most promising materials for NW photodetectors, due to their excellent transport properties, ease of doping, and the possibility to tune their optical absorption over a wide spectral range by alloy bandgap engineering. Photoconductive response of single III-arsenide NWs are characterized by conductive atomic force microscopy (Xia et al., 2012) and on-chip time-resolved photocurrent pump-probe spectroscopy (Erhard et al., 2013; Prechtel et al., 2012). The latter method was used to analyze photoinduced thermoelectric displacement, carrier lifetime limited currents, and the transport of photogenerated holes to the electrodes in single GaAs and InAs NWs. Single NW photodetectors were also demonstrated in InAs NWs with a photoresponse over a broad spectral range from 300 to 1100 nm, showing high responsivity, external quantum efficiency and detectivity respectively of 4.4×10^{3} A W^{-1}, 1.03×10^{6}%, and 2.6×10^{11} Jones at 532 nm (Liu et al., 2013). Since the

Table 1 Basic Parameters of Compound Semiconductor Used in Photodetectors

	InSb	InAs	InP	GaAs	GaP	CdS	ZnSe	ZnO	GaN	ZnS	AlN
E_g (eV)	0.17	0.354	1.344	1.43	2.27	2.50	2.82	3.35	3.39	3.60	6.2
Electron mobility ($cm^2\ V^{-1}\ s^{-1}$)	77,000	40,000	5400	8500	350	340			1000	165	135
Hole mobility ($cm^2\ V^{-1}\ s^{-1}$)	850	500	200	400	100	340			30	5	14
Dielectric constant	16.8	15.15	12.5	12.5	9.7			9.1	8.9	9.6	8.5

carrier distribution inside the NW is mainly determined by the surface potential and Fermi energy pinning, which strongly depend on the geometry of the wire, the dark- and photocurrents in NWs vary considerably with their size. Theoretical calculations for InP NWs have shown that small diameters (i.e., minimal band bending) result in full-depletion of the NWs, thus minimizing the dark current (the predominant source of noise in photodetectors), while large diameters (i.e., appreciable band bending) increase the photoconductivity by hindering photogenerated carrier recombination (Wang and Asbeck, 2006). Fast (14 ps FWHM at 780 nm) photoconductive response has been demonstrated in an intersecting array of InP NW grown in a coplanar waveguide transmission line (Logeeswaran et al., 2008). These studies have highlighted the potential of III–V compound semiconductor NWs for the fabrication of high-speed photodetectors.

2.3.2 Nitride Nanowire Photoconductors

III-nitride NWs are attracting increasing attention for ultraviolet and visible range photodetection. The most studied material is GaN; however, InGaN/GaN (Bugallo et al., 2011; Erhard et al., 2015) and GaN/AlN heretostructures (Martien den et al., 2013; Rigutti et al., 2010b) have also been investigated. The early studies of photoconduction in GaN NWs have revealed some problems, such as persistent photoconductivity effects (Han et al., 2004) and defect-related photocurrent in the visible range (Polenta et al., 2008). However, growth optimization and a careful design of the NW diameter and doping allow to eliminate these drawbacks and to greatly improve the device performance with respect to the thin-film case (Gonzalez-Posada et al., 2012). For example, a photoconductive gain of 10^5–10^7 has been reported in *m*-axial and *c*-axial single GaN NWs leading to a very high responsivity (Chen et al., 2007; Gonzalez-Posada et al., 2012). An example of a single GaN NW detector with an n–i–n axial junction is shown in Fig. 2A–C. The photoconductive gain of the detector is in the 10^6 range, and is shown to decrease with modulation frequency and with incident power. The photocurrent response dependence on the incident light polarization follows the $\cos^2\vartheta$ law described by Eq. (12) of Section 2.2.1. These GaN NW detectors have shown six orders of magnitude UV-to-visible contrast. A photocurrent time response in the millisecond range has been achieved in these structures, in contrast to the persistent (hours) photoconductivity effects observed in two-dimensional GaN photoconductors (Gonzalez-Posada et al., 2012).

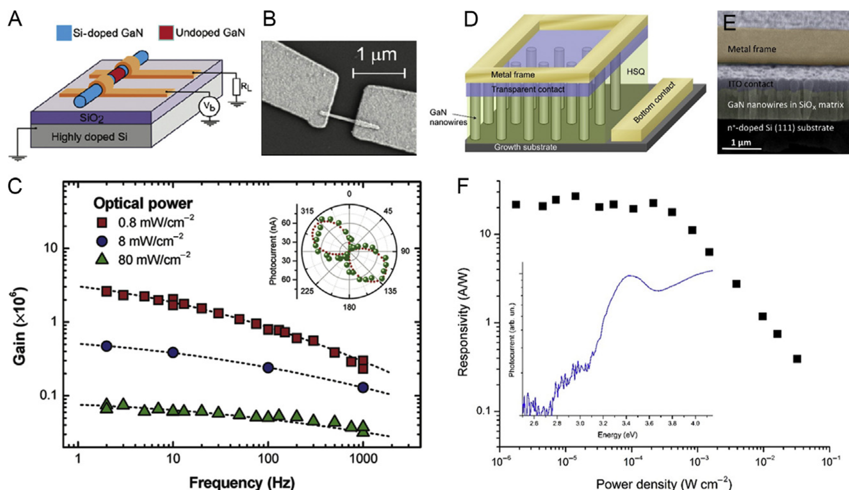

Figure 2 GaN single NW photodetector (A) schematic, (B) SEM image, and (C) Gain over frequency dependence for different excitation powers. Inset shows the polarization anisotropy of the detector. GaN NW array photodetector (D) schematic, (E) SEM image in artificial colors, and (F) dependence of the responsivity on the excitation power. Inset shows the photocurrent spectrum. *Panels (A–C) Adapted with permission from Gonzalez-Posada et al. (2012). Copyright (2012) American Chemical Society. Panels (D–F) Adapted with permission from Babichev et al. (2013).*

GaN NWs have shown strong sensitivity to the ambient conditions (e.g., air vs. vacuum; Rigutti et al., 2010a). This is a signature that the high surface-to-volume ratio plays a key role in the NW transport and photoconduction. As pointed out earlier, surface states play a major role in determining the effective conduction surface in the NW, the photocarrier lifetime, and ultimately the NW photoconductive response. As a result, the photocurrent density strongly depends on the NW diameter, as was reported by many groups in GaN NWs (Calarco et al., 2005; Chen et al., 2011). This dependence has been interpreted in terms of a surface pinning barrier model. Surface states lying within the forbidden gap are known to induce a surface Fermi level pinning and to cause a depletion region close to the surface. The surface depletion layer induces a spatial separation of the photogenerated electrons and holes along the NW radius. The depletion layer can extend over an important part of the wire thickness or even over its whole volume, depending on the wire diameter and doping (Calarco et al., 2005). The model of Calarco et al. has been further developed by Sanford et al. (2010, 2013) to rigorously calculate the NW band bending profile and also to describe the photocurrent slow decay. The presence of a surface

barrier and of a consequent band bending of the semiconductor energy bands has been confirmed by the observation of a diameter-dependent Franz–Keldysh effect in the photocurrent spectra of GaN NWs (Cavallini et al., 2007).

Most of the GaN NW photoconductor detectors reported in the literature are based on single NWs, with only few reports on array devices (Babichev et al., 2013; Wu et al., 2009). Figure 2D–F shows an example of a photodetector based on an array of vertical GaN NWs. As schematized in panel *d*, the NWs are kept on their growth substrate (conductive Si (111)), partly encapsulated into a spin-on glass and top-contacted with a transparent conductive material (such as ITO or graphene; Babichev et al., 2013). The detector shows a photoresponse restricted to the UV spectral range. The responsivity decreases for high incident power densities. In general, the reported responsivity (below 100 A W^{-1}) and the photoconductive gain for array detectors remain lower than for single NW devices. Further technological optimization in terms of wire-to-wire homogeneity and processing technology is required to fully benefit from the NW properties in ensemble-based photoconductors.

2.3.3 Group II–VI

II–VI semiconducting compounds (metal-oxides, sulfides, selenides, and tellurides) are widely employed in optoelectronic applications due to their wide coverage of bandgap energies. The strong influence of surface chemistry on the conductive and photoconductive properties of metal-oxide NWs makes them especially suitable for gas and chemical sensing. Among them, ZnO is one of the most interesting NW materials in visible-blind UV photodetectors due to the wide bandgap ($E_g = 3.34$ eV at room temperature). Additionally, the presence of oxygen vacancies sometimes results in deep level donor states manifested in a "green" photoluminescence and photoconductivity band, which may be exploited to extend the spectral sensitivity of ZnO to the visible range (inset of Fig. 3A). The studies of the photoconductivity of ZnO NWs have revealed a photoconductive gain as high as $G \sim 10^8$ (Fig. 3B). Despite the slow relaxation time ($\tau \sim 10$ s), the extremely high photoconductive gain resulted in gain-bandwidth products of GB > 10 GHz, as confirmed by the fast photocurrent response measured in the subnanosecond time domain (Soci et al., 2007). Other analyses of photoconductivity in ZnO NWs have confirmed these results (Prades et al., 2008b). Large photoconductive gain is achieved at the expense of dynamic response, although optimization of the electrode geometry to

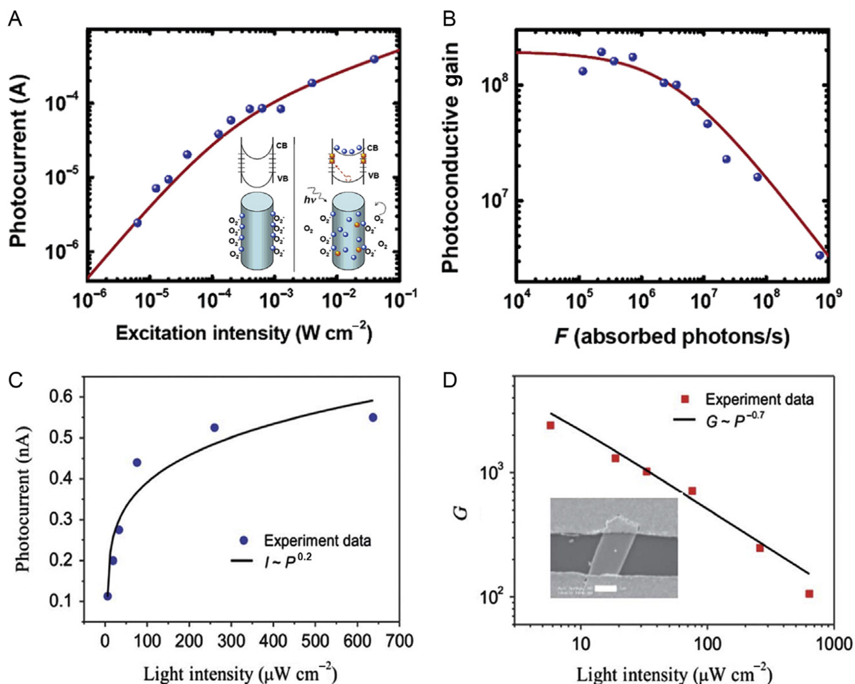

Figure 3 (A) Photocurrent of a single ZnO NW device measured as a function of excitation intensity ($\lambda = 390$ nm) with 5 V applied bias. Inset shows schematic of the energy band diagrams, adsorption, and desorption of oxygen molecules on a NW in dark and under illumination. (B) Estimate of the photoconductive gain relative to the photon absorption rate in the ZnO NW. (C and D) Dependence of gain and responsivity on light intensity of a CdTe nanoribbon ($\lambda = 400$ nm). *(B) Adapted with permission from Soci et al. (2007) Copyright (2007) American Chemical Society. Panels (C and D) Reproduced from Xie et al. (2012), reproduced with permission of the Royal Society of Chemistry.*

minimize carrier transit time can allow achieving simultaneously high sensitivity and large gain-bandwidth products.

Lower bandgap II–VI materials, such as CdS, CdSe, ZnSe, CdTe, and ZnTe, are typically used for visible light detection. CdS NWs and nanobelts are among the most studied photoconductors in group II–VI for visible and ultraviolet light detection (Deng and Li, 2014). Similar to the case of metal-oxide NWs, the photoresponse of CdS low-dimensional structures is strongly affected by surface oxygen photochemistry, which can significantly alter the photocarrier relaxation dynamics (Jie et al., 2006). The photoconductive properties of CdSe nanobelts have also been investigated in both intrinsic and n-doped structures. Fast speed (response/recover times ~15/31 μs) and high photosensitivity (~100) were observed in i-CdSe,

while high-gain is preserved in n-CdSe. These differences result mainly from impurity induced traps inside the nanobelts (Wu et al., 2011). In the visible-NIR range (400–800 nm), CdTe nanoribbons with p-type conductivity presents significant photoresponse to irradiation with high responsivity and gain of 7.8×10^2 A W^{-1} and 2.4×10^5%, respectively (Fig. 3C–D; Xie et al., 2012). For infrared detection, $Hg_{1-x}Cd_xTe$ is one of the most important semiconductor materials since its bandgap can vary monotonically over a wide spectral range, from the far-infrared to 1.5 eV.

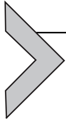

3. PHOTOTRANSISTORS

A phototransistor is a bipolar or unipolar transistor where light can reach the base, creating optically generated carriers. This modulates the base-collector junction resulting in an amplified current through transistor action, which can lead to much greater photosensitivity.

Typically, NW field-effect transistors (FETs) have been fabricated dispersing NWs on a dielectric-semiconductor substrate (Ahn and Jiwoong, 2007; Arnold et al., 2003; Han et al., 2004; Heo et al., 2004a; Li et al., 2004; Ye et al., 2010; Zhang et al., 2003) or by patterning NWs through conventional lithographic methods. Subsequently, a gate bias is applied through a lithographically patterned top gate, or a back gate. A high-performance CdS nanobelt metal-semiconductor FET (Fig. 4A) exhibited an ultrahigh photoresponse ratio with I_{light}/I_{dark} of 2.7×10^6, high current responsivity of 2.0×10^2 A W^{-1}, high external quantum efficiency of 5.2×10^2, and fast rise and decay time of 137 and 379 μs (Fig. 4B). Such good properties were achieved by applying a gate voltage near the threshold voltage under illumination, which was more negative than the threshold voltage in the dark. This facilitated the depletion of the channel carriers, constrained the long decay time and led to a fast photoresponse (Ye et al., 2010).

In the case of these FET photodetectors, an electrical gate bias is used to modulate the lateral field across the NW. However, a similar effect is also present in NW photoconductors in which surface states give rise to a radial electric field. This causes the separation of photogenerated carriers in the NW channel, which greatly extends the carrier recombination lifetime leading to a much higher sensitivity. Thus, NW photoconductors can be viewed as phototransistors where the internal field arising from the large density of surface states in conjunction with light illumination act as a photogate. Depending on the NW material, band bending can be caused by different

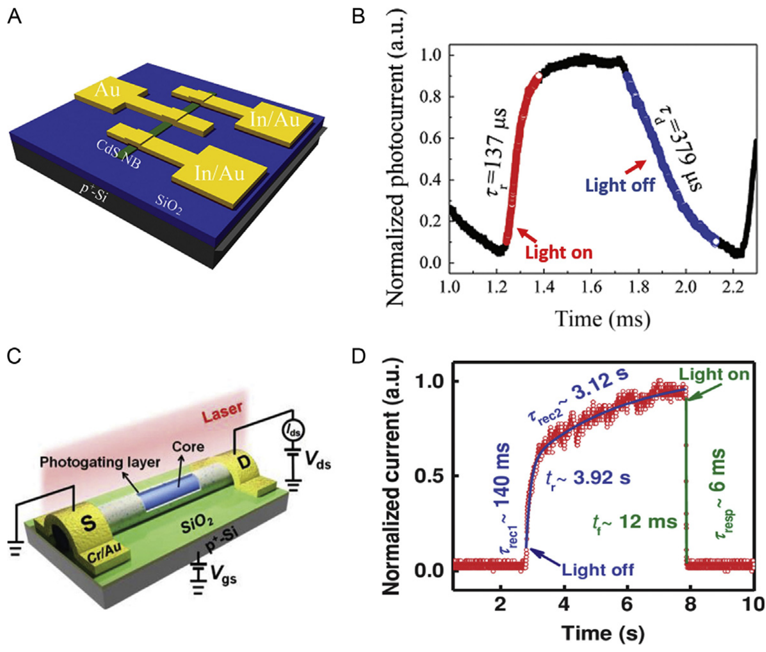

Figure 4 (A) Schematic illustration of a single CdS nanobelt MESFET-based photodetector. (B) Transient photocurrent response of (A) at $V_G = -3.8$ V and $V_{DS} = 0.5$ V. (C) A schematic of the InAs NW transistor with a self-assembled photogating layer. (D) A single normalized modulation cycle measured with $V_G = 0$ V and $V_{DS} = 1$ V. *Panels (A and B) Adapted with permission from Ye et al. (2010). Copyright (2010) American Chemical Society. Panels (C and D) Adapted with permission from Guo et al. (2014).*

surface mechanisms, such as the presence of a strong surface electric field (as in GaN NWs; Calarco et al., 2005; Reui-San et al., 2007), the presence of deep trap states (for instance, oxygen-related hole traps in ZnO NWs; Soci et al., 2007), or the surface defect states (such as in InAs NWs; Miao et al., 2014).

In general, most of the NW phototransistors nowadays are based on minority carrier transport and suffer from recombination before carrier collection by the contacts. In comparison, a core/shell-like n-InAs NW phototransistor (Fig. 4C), with a self-assembly photogating layer containing randomly distributed lattice defects as trapping centers to capture photoexcited electrons, was demonstrated for the majority carrier transport (Guo et al., 2014). Upon illumination, electrons are excited to and trapped in the photogating layer; holes are recombined with free electrons in the core, leading to a low light current. In the dark, most of the trapped electrons are

released and form a high dark current. Such device demonstrates a high photoconductive gain ~10^5 and a fast response time of 12 ms (Fig. 4D; Guo et al., 2014).

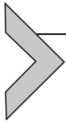

4. NANOWIRE HETEROSTRUCTURES

After the early interest in large photoconductive gain of NW photoconductors due to their inherently large surface-to-volume ratio, NW heterostructures are now actively investigated for efficient conversion of optical to electrical signals in integrated photonic circuits. In the following, we discuss some of the most promising heterostructured NW architectures adopted from thin-film compound semiconductor photodetector technologies, including homogeneous, inhomogeneous, Schottky junction photodiodes, and avalanche photodetectors (Fig. 5).

4.1 Homogeneous and Heterogeneous Photodiode Junctions

Photodiode junctions (e.g., semiconductor p–n or p–i–n photodiodes) are being successfully replicated in NW structures, where homo- and hetero-junctions are either formed directly during the NW growth (bottom-up approach) or prior to the NW fabrication (top-down approach). Note that recently a lot of interest has arisen for NW photodiodes operated in photovoltaic mode for solar power conversion. Single NW solar cells have been experimentally realized in homojunctions (such as GaAs radial p–i–n NW (Krogstrup et al., 2013) and GaAsP radial p–i–n NW (Holm et al., 2013)), heterostructured GaAs/InGaP/GaAs core–multishell NW (Gutsche et al., 2012),

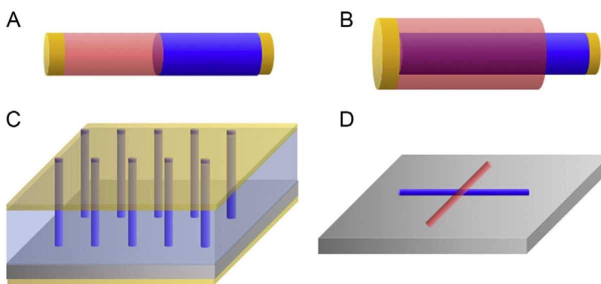

Figure 5 (A) Axial NW junction, (B) core/shell, radial NW junction, (C) vertical NW array heterojunctions formed with the growth substrate, and (D) "crossed" NW junction. The segments in different colors represent either different doping or different materials for homogeneous and heterogeneous junctions, respectively. *Adapted from Soci et al. (2010).*

and Schottky contacted GaAs NW (Han et al., 2012). Vertical NW array heterojunctions (such as n-GaAs NWs/n^{+}-Si (Hu et al., 2013) and n-InAs/p-Si (Wei et al., 2009)) and vertical NW arrays of homo- and hetero-junctions (such as axial InP p-n junction on InP substrate (Wallentin et al., 2013), n-core/p-shell GaAsP n-p junction on Si substrate (Tchernycheva et al., 2012), n-core/p-shell GaAs NWs on n-GaAs substrate (Czaban et al., 2009), or ZnO-core/ZnSe-shell NWs on transparent conductive oxide substrate (Wang et al., 2008)) have been explored. For the sake of brevity, studies specifically aimed at photovoltaic applications will not be discussed here, whereas we will focus on NW photodiode structures used for photodetector applications.

p-n and p-i-n structures are among the most common architectures for homo- and heterojunction NW photodiodes. The p-n/p-i-n junction is usually operated under reverse bias to minimize the dark current. As illustrated in Fig. 6, electron–hole pairs (EHP) generated by the photon absorption in the vicinity of the intrinsic or charge depletion regions are separated by the internal electric filed and create a negative photocurrent. The external reverse bias increases the barrier height of the junction and the width of charge depletion region, resulting in more efficient separation of EHPs thanks to the increased electrical field in the junction.

Both axial homo- and heterojunction NW photodiodes (Fig. 5A) have been demonstrated. For instance, UV photodetectors based on single GaN NWs including axial p-n homojunctions have shown rectifying behavior, relatively fast photoresponse, and a photoconductive increase of about

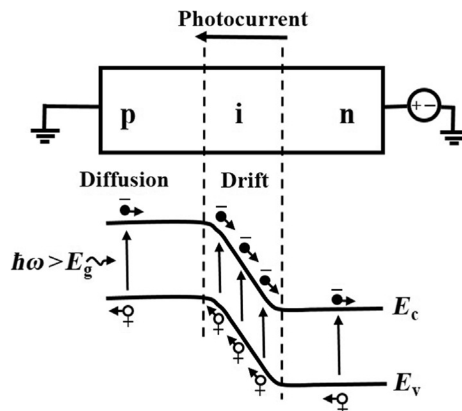

Figure 6 Energy band diagram and mechanism of photocurrent generation in a p-i-n photodiode.

14 under 0.03 V reverse bias (Son et al., 2006). Photodetectors based on NW ensembles have been demonstrated making use of a p-i-n junction within the GaN NWs (Jacopin et al., 2014). Compared to thin-film GaN p-i-n detectors, which present good performance in terms of operation speed, power linearity, and detectivity (Monroy et al., 2003), NW p-i-n photodiodes show a slower response, nonlinear power dependence and may present an internal gain (Jacopin et al., 2014). Indeed, for axial p-i-n junction NW devices, the p- and n-doped segments display photoconductive effects following the mechanism described in Section 2.1. Because of the leakage current in the junction region, which is attributed to the hopping through surface states, these photoconductive effects become predominant under bias.

Similarly, IR photodetectors based on single NWs of InAs/InAsP axial heterojunctions operated at 77 K exhibited very low dark current (due to the conduction band offset formed at the NW heterointerface), strong polarization dependence, and a combined contribution to the photoconductive response from the InAs portion (with onset around 0.5 eV) and from the InAsP portion (with tunable onset from 0.65 to 0.82 eV depending on the phosphorous content; Pettersson et al., 2006). High selectivity to spatial and linear polarization has also been observed in a InP NW photodetector with a single InAsP quantum dot, possessing a quantum efficiency of 4% and NEP of 10^{-13} W Hz$^{-1/2}$ (van Kouwen et al., 2010).

As mentioned earlier, core–shell NW junctions (Fig. 5B) are attracting a lot of interest for photovoltaic applications, although similar design concepts could be implemented for more efficient photosensing schemes that take advantage of the more effective charge carrier separation, and possibly of the enhanced light absorption in vertical arrays expected from radial NW junctions (Kayes et al., 2005). So far, photoresponse of GaAs system has been widely investigated, including GaAs/AlGaAs core–shell (Dai et al., 2014; Gallo et al., 2011; Jiang et al., 2013; Kim et al., 2013; Persano et al., 2011), and GaAs/InGaP/GaAs core–multishell NWs (Gutsche et al., 2012). Among them, the NIR photodetector based on a core–shell GaAs/AlGaAs NW exhibited a remarkable peak photoresponsivity of 0.57 A W^{-1} at room temperature, comparable to large-area planar commercial GaAs photodetectors, and a high detectivity of 7.2×10^{10} cm Hz$^{1/2}$ W^{-1} at $\lambda = 855$ nm (Dai et al., 2014). Type-II core/shell NW heterostructures have also been proposed (Zhang et al., 2007) and demonstrated (Wang et al., 2008) to promote charge carrier separation, improve the photosensitivity and additionally enhance the spectral response. InGaN/GaN core/shell

p–i–n diodes for visible-to-UV detection have been reported (Tchernycheva et al., 2014) as illustrated in Fig. 7. The structure schematized in Fig. 7A consists of an n-type GaN core, undoped InGaN radial segment absorbing visible light and a p-doped GaN shell. The n-doped core remains uncovered at the NW base part allowing to contact the n- and p-layers without additional etching steps (see the SEM image of the processed device shown in inset of Fig. 7C). The responsivity of the detector extracted from the current–voltage characteristics in the dark and under illumination with $\lambda = 400$ nm (Fig. 7B) is 0.075 A W^{-1} at zero bias. The photocurrent spectrum shown in Fig. 7C increases starting from 2.8 eV corresponding to the absorption of the InGaN layer and extends to the UV range.

Photodetectors based on heterogeneous junctions formed by vertical NW arrays with their growth substrates (Fig. 5C) have also been investigated, where large NW densities are desirable to increase the photoactive area and thus enhance the photoconductive response. In particular, due to the ease of fabrication by a variety of methods, including chemical vapor deposition, solvothermal methods, or magnetron sputtering, a substantial amount of work has been dedicated to heterojunction photodetectors made of ZnO NWs on doped Si substrates. In these structures, depending on the density of the NW network, the top electrode can be either deposited directly onto the NW layer or a transparent filling material such as spin-on-glass or an inert polymer can be used to reduce leakage current. Intrinsically doped, n-type ZnO NWs have been grown on both, p-type or n-type Si substrates, where the dependence of the dark current on applied bias is

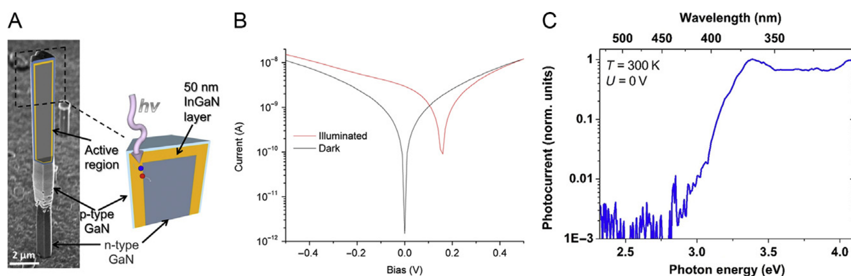

Figure 7 (A) Schematic of the internal structure of the core/shell InGaN/GaN NW photodetector illustrated on an SEM image of a typical wire. (B) *I–V* curves of the detector in the dark and under illumination. (C) Photocurrent spectrum of a NW detector. Inset shows an SEM image of a contacted NW. *Adapted with permission from Tchernycheva et al. (2014). Copyright (2014) American Chemical Society.*

found to resemble the ideal relationship for heterojunctions, with typical rectifying behavior (Sze, 1981):

$$I = I_s \left[\exp\left(\frac{eV}{k_B T} \right) - 1 \right] \tag{13}$$

where I_s is the saturation current and the other symbols have their usual meaning. In the case of the n-ZnO NW/p-Si heterojunction, photoconductivity studies performed under UV light illumination and reverse bias have shown responsivity of ~0.07 A W^{-1} at −20 V applied bias (Luo et al., 2006), with fast and slow components of the photocarrier dynamics of the order of ~300 ms and few minutes, respectively (Ghosh and Basak, 2007). Interestingly, in the case of n-ZnO NW/n-Si heterojunction, the spectral sensitivity could be tuned from the visible to the ultraviolet spectral regions by applying forward or reverse bias to the device, by controlling the band offset at the heterointerface and by selectively collecting photocarriers that are generated in the Si substrate, or in the ZnO NWs, respectively (Zhen et al., 2008).

Similarly, NIR photodetector based on axial n$^+$-i-InP NW arrays on p$^+$-InP substrate has been demonstrated with an outstanding rectifying behavior with an ideality factor of about 2.5 at room temperature and small leakage current at −1 V. The photocurrent was mainly generated by funneling photogenerated carriers from the substrate into the NWs at room temperature, while the direct excitation of NWs became dominated at low temperatures (Pettersson et al., 2012). Further experiments in n$^+$-i-p$^+$ InP NW arrays have demonstrated that the photocurrent generation process depended strongly on the length of p$^+$-region, resulting in the formation of a well-defined electric filed confined in the i-region of the NWs (Jain et al., 2015). Recent advances in the direct heteroepitaxial growth of III–V NWs on Si will also open up new opportunities for vertical NW array photodetectors and photovoltaics (Bao et al., 2008; Shin et al., 2013).

4.2 Schottky Junctions

Schottky photodiode uses a metal/semiconductor junction to separate and collected the photogenerated carriers. EHP generated in the vicinity of the depletion region are swept out by the built-in field of the Schottky junction. One of the advantages of Schottky photodiodes is the fast response speed, due to the high electric field (thus the short carrier transit time) across the junction under reverse bias. The current in an ideal Schottky diode is still

given by Eq. (13), with the reverse bias saturation current given by Sze (1981):

$$I_s = A^* T^2 \exp\left(-\frac{e\phi_b}{kT}\right) \quad (14)$$

where A^* is Richardson's constant and ϕ_b is the Schottky barrier height. To account for the deviation from the ideal behavior, Eq. (13) is further modified as Milnes and Feucht (1972):

$$I = I_s\left[\exp\left(\frac{e(V - V_{th})}{nk_B T}\right) - 1\right] \quad (15)$$

in which V_{th} is the forward-bias threshold voltage, and n the ideality factor. When the current is dominated by thermionic emission over the Schottky barrier $n = 1$.

The effects of Schottky barriers at the metal–semiconductor interface on the photogenerated carrier separation and transport are often encountered in the literature of semiconductor NWs. In particular, scanning photocurrent microscopy (SPCM) has proven a valuable tool for the investigation of these effects in NW photodetectors. In SPCM experiments conducted on CdS (Dufaux et al., 2012; Gu et al., 2006) and CdSe NWs (Doh et al., 2008), photocurrent–voltage characteristics were typically asymmetric and, depending on the biasing conditions, photocurrent could be strongly localized near the metal electrode-NW contact. The SPCM technique is very effective to investigate the mechanisms of photodetection at the nanoscale, such as mapping the electronic band profile along the NW axis (Ahn et al., 2005; Doh et al., 2008), determining the carrier mobility-lifetime products (Gu et al., 2006), or analyzing the electron recombination behavior of the wires (Dufaux et al., 2012).

Despite the good understanding of metal-semiconductor junctions in NW devices, the investigation of Schottky photodiodes has been pursued in materials including ZnO NWs/nanobelts (Cheng et al., 2008; Zhang et al., 2006b), CdS NWs/nanobelts (Dufaux et al., 2012; Wei et al., 2010), SiC NWs (Peng et al., 2015), GaN NWs (González-Posada et al., 2013; Wang et al., 2014), GaAs NWs (Dai et al., 2014), and InSb NWs (Kuo et al., 2013).

In case of asymmetric contacts (i.e., one Ohmic contact and on Schottky contact), ideality factors of ZnO NW Schottky photodiodes extracted by using Eq. (15) are often considerably larger than unity, due to the influence

of both interface and surface states (Cheng et al., 2007; Harnack et al., 2003). However, an almost ideal Pt/ZnO NW Schottky junction photodiode could also be demonstrated (Heo et al., 2004b).

Two-terminal NW devices with symmetric contacts made of noble metals (such as Au, Ag, and Pd) usually behave as back-to-back Schottky diodes (metal–semiconductor–metal diodes, MSM). In the dark, thermionic emission primarily determines and limits the current transport of MSM photodetector (Nabet et al., 2003). Under illumination, the increment of carrier density enhances the tunneling probability across the Schottky barrier at the metal/semiconductor interface, where the self-built potential plays a crucial role in the carrier separation and transport, especially when it is reverse-biased (Gu et al., 2005). Such MSM structure has been used in a core–shell GaAs/high-T GaAs/AlGaAs (40/170/30 nm) NW with Pt contacts on the GaAs core and AlGaAs shell, respectively. The electron distribution in the cross section of this NW was mapped by solving self-consistent Schrödinger–Poisson equations, indicating the electron confinement at the GaAs/AlGaAs heterointerface (Fig. 8A). The corresponding core–multishell NW is shown in Fig. 8B with a total radius of around 240 nm and hexagonal cross section. Figure 8C compares the representative I–V characteristics in the dark and under illumination. An asymmetric I–V curve with low dark current was measured, limited by the different Schottky barrier heights between Pt/GaAs and Pt/AlGaAs in the MSM structure. The dark current is successfully suppressed in this case. Under illumination, the photocurrent was found to increase rapidly in the voltage range of −1 to 1 V, and then to increase at a lower rate. When a contact is under reverse bias, its Schottky barrier height increases, providing a stronger local built-in electric filed at the contacts. Thus, photogenerated electrons and holes are efficiently separated by this field, increasing the photocurrent. The maximum current is limited by carrier drifting in the space-charge region near the contact and GaAs/AlGaAs heterointerface, and diffusion inside the neutral region of the NW (carrier diffusion length and lifetime). Under negative bias of −2 V and positive bias of 2 V at the AlGaAs shell with GaAs core grounded, a maximum current of −0.8 and 0.62 nA was produced. The different current values originate from the higher Schottky barrier height at Pt/AlGaAs interface than at Pt/GaAs interface, leading to a clear photocurrent to dark current on/off ratio. Figure 8D shows the measured photoresponsivity spectrum, similar to a typical GaAs photordetector except for the appearance of few peaks. This indicates that absorption occurs in the GaAs core rather than in the AlGaAs shell and suggests the presence of

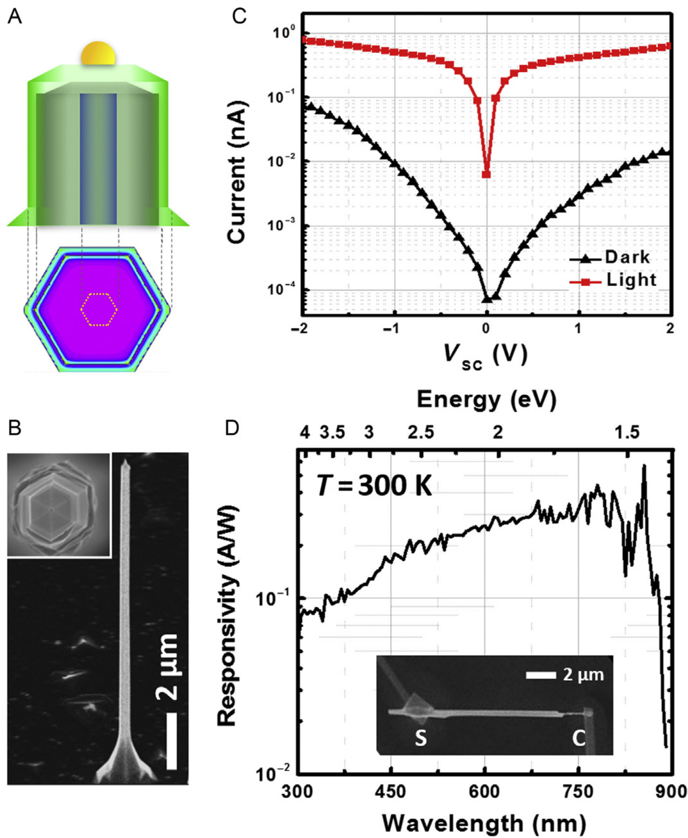

Figure 8 (A) Schematic of a core-multishell GaAs/high-T GaAs/AlGaAs NW (40/170/30 nm). Contour plot shows the simulated spatial distribution of electron concentration in the cross-sectional plane. (B) Corresponding SEM image of NW in (A) obtained with a tilt angle of 45°. The inset is a top-view image of the core-multishell NW showing its hexagonal cross section. (C) Current–voltage relationship of a core-multishell NW in the dark and under Xe lamp illumination. (D) Experimental photoresponsivity as function of the excitation wavelength for a core-multishell NW photodetector at room temperature under a bias of 2 V: peaks can be observed on a typical GaAs photoresponse. The inset is a SEM image of the device with one contact on the core and one on the shell. *Adapted with permission from Dai et al. (2014). Copyright (2014) American Chemical Society.*

optical resonant modes within the NW leading to an absorption enhancement. At $\lambda = 855$ nm, responsivity, defined as the ratio of electrical output to the optical input, is 0.57 A W^{-1}, which is higher than the commercial GaAs photodetector. Specific detectivity is 7.20×10^{10} cm $Hz^{1/2}$ W^{-1}, slightly lower than the values reported for planar GaAs photodetectors. As a result,

the radial charge separation promoted by the core–shell structure with MSM configuration decreases carrier recombination and increases the total photocurrent, demonstrating the feasibility of such design for efficient NW photodetectors (Dai et al., 2014).

4.3 Avalanche Photodiodes

One of the most interesting implementations of NW photodetectors is given by avalanche photodiodes (APDs), where operation at large reverse bias allows each photogenerated carrier to be multiplied by avalanche breakdown caused by band-to-band carrier impact ionization. Carrier multiplication results in internal gain within the photodiode, which increases the effective responsivity of the device. The figure of merit for this process is the multiplication factor (or gain) M, which indicates the average number of carriers produced from the initial photocarriers (Driggers, 2003):

$$M = \frac{1-k}{e^{-\delta(1-k)} - k}, \quad k = \beta(E)/\alpha(E) \tag{16}$$

where δ is the average number of ionization events per electron transit, and α and β are the field-dependent ionization rates for electrons and for holes, respectively. So far, NW APDs have been demonstrated in three different configurations, namely a "crossed" n-CdS/p-Si NW heterojunction (Hayden et al., 2006) (Fig. 5D), an axial p-i-n single Si NW homojunction (Reimer, 2011; Yang et al., 2006) or an InAsP QD in axial InP p-n junction (Bulgarini et al., 2012; Fig. 5A), and a radial GaAs nanoneedle junction (Chuang et al., 2011) or a radial GaAs p-n junction (Senanayake et al., 2012; Fig. 5B).

In the case of the n-CdS/p-Si "crossed" APD, a photocurrent increase (I_{PC}/I_{dark}) of $\sim 10^4$ times higher than in individual n-CdS or p-Si NW photoconductors has been observed due to avalanche multiplication at the p-n crossed NW junction, with multiplication factors as high as $M = 7 \times 10^4$. Polarization dependence of the photoresponse has also been observed in the "crossed" structure, due to the predominant optical absorption in the CdS NW, as verified by spectral measurements. A detection limit of about 75 photons was estimated for these devices (Hayden et al., 2006). Very similar results (namely polarization sensitivity, high spatial resolution, and high sensitivity) were obtained in the case of the axial p-i-n Si NW APD, where complementary doping within a single NW was used instead of the assembly of two distinctly doped NWs. A maximum multiplication factor of $M = 40$ was derived in this case. Interestingly, multiplication factors

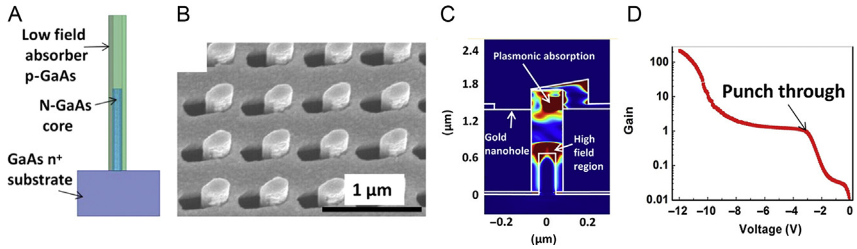

Figure 9 (A) Schematic of the single APD. (B) Self-aligned metal nanohole lattice for plasmonically enhanced absorption. (C) Contour plot of plasmonically enhanced photogeneration and electrical filed in nanopillars at −10 V. (D) The multiplication of the APD. *Adapted with permission from Senanayake et al. (2012). Copyright (2012) American Chemical Society.*

for electron and hole injections could also be isolated, indicating that the multiplication factor for electrons ($M_n < 100$) was larger than that for holes ($M_p < 20$) due to larger electron ionization rate ($\alpha > \beta$) (Yang et al., 2006). High multiplication factor ($>10^4$) was also observed in an InP NW with a single InAsP QD, which acted as the only absorption region and allowed the generation of a single exciton for tunneling and multiplication of carriers into a NW APD (Bulgarini et al., 2012). First demonstration of GaAs-based APD was realized in radial p-n GaAs nanoneedles grown on an n-Si substrate. Photocarriers were generated in both nanoneedles and Si substrate, collected and multiplied by the nanoneedles subsequently. The multiplication factor lower band ($\delta = 100\%$) reached 29 at −2 V and 263 at −8 V. The mechanism of avalanche multiplication was attributed to the high electric field inside the tapered nanoneedle (Chuang et al., 2011). Similar configuration of electrical contacts was utilized in selectively grown radial p-n GaAs NW array, forming a self-aligned metal nanohole lattice for plasmonically enhanced absorption via surface plasmon polariton Bloch wave modes (Fig. 9A–B). A confined 3D electric field formed in the junction was within avalanche path length of carriers and acted as the multiplication region, promoting an avalanche gain of ~216 at 730 nm at −12 V (Fig. 9C–D) (Senanayake et al., 2012).

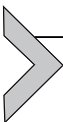

5. SUMMARY AND CONCLUSIONS

In this chapter, we gave an overview on different compound semiconductor NW photodetector concepts and realizations. We have shown that one-dimensional or quasi-one-dimensional nanostructures offer several

advantages for photodetection over their bulk or thin-film counterparts, namely: (i) dense device integration and sub-wavelength spatial resolution, (ii) enhanced light absorption with a small amount of active material in NW arrays, (iii) discrimination of light polarization, (iv) large photosensitivity due to internal photoconductive or phototransistive gain, (v) possibility to integrate functionality within single NW devices (e.g., photodiodes, heterostructured devices, etc.), and (vi) heterogeneous integration of NWs and substrates of different materials for enhanced or specific spectral sensitivity.

Besides the extremely interesting fundamental properties of these low-dimensional nanostructures from the physics and materials science standpoints, NW photodetectors are now gaining enormous significance in device engineering. Particularly in the emerging fields of integrated nanophotonics and quantum optics, availability of extremely sensitive (down to the single photon level), wavelength scale, integrated photodetectors is of paramount importance. Proof-of-concept realizations of integrated photonic circuit employing NWs as light sensing elements have already been demonstrated: a nanostructured GaAs photodetector coupled to a metal nanoparticle within its near field provided efficient transduction (De Vlaminck et al., 2007); an optical communication between InGaN/GaN NW emitter and detector coupled by a waveguide was demonstrated (Tchernycheva et al., 2014); a Ge NW photodetector crossed with a silver NW plasmonic waveguide generated EHPs when surface plasmon polaritons were introduced and exhibited a responsivity up to 50 electrons per plasmon (Falk et al., 2009). Plasmonic enhanced detectors have also been realized in the material systems of InGaAs nanopillars (Senanayake et al., 2011), Si NWs (Luo et al., 2014), and Si pyramids (Desiatov et al., 2015). Together with the availability of integrated NW laser sources (Couteau et al., 2015), we therefore envision that compound semiconductor NWs photodetectors will play a central role in the next stage of the photonic revolution, for high resolution optical imaging, high-speed and low-energy signal processing, as well as for biological or chemical photometric sensing.

ACKNOWLEDGMENTS

We are grateful to A. Messanvi, A. Zhang, C. Wilhelm, H. Zhang, G. Jacopin, and P. Lavenus whose Ph.D. work is partly described in this review, and to C. Durand, D. Wang, J.-C. Harmand, J. Eymery, L. Rigutti, L.W. Tu, S.A. Dayeh, and Y.H. Lo who collaborated with us on particular topics.

REFERENCES

Ahn, Y.H., Jiwoong, P., 2007. Efficient visible light detection using individual germanium nanowire field effect transistors. Appl. Phys. Lett. 91, 162102.

Ahn, Y., Dunning, J., Park, J., 2005. Scanning photocurrent imaging and electronic band studies in silicon nanowire field effect transistors. Nano Lett. 5, 1367–1370.

Arnold, M.S., Avouris, P., Pan, Z.W., Wang, Z.L., 2003. Field-effect transistors based on single semiconducting oxide nanobelts. J. Phys. Chem. B 107, 659–663.

Babichev, A.V., Zhang, H., Lavenus, P., Julien, F.H., Egorov, A.Y., Lin, Y.T., Tu, L.W., Tchernycheva, M., 2013. GaN nanowire ultraviolet photodetector with a graphene transparent contact. Appl. Phys. Lett. 103, 201103.

Bao, X.Y., Soci, C., Susac, D., Bratvold, J., Aplin, D.P.R., Wei, W., Chen, C.Y., Dayeh, S.A., Kavanagh, K.L., Wang, D.L., 2008. Heteroepitaxial growth of vertical GaAs nanowires on Si (111) substrates by metal-organic chemical vapor deposition. Nano Lett. 8, 3755–3760.

Bube, R.H., 1960. Photoconductivity of Solids. Wiley, New York.

Bugallo, A.D.L., Rigutti, L., Jacopin, G., Julien, F.H., Durand, C., Chen, X.J., Salomon, D., Eymery, J., Tchernycheva, M., 2011. Single-wire photodetectors based on InGaN/GaN radial quantum wells in GaN wires grown by catalyst-free metal-organic vapor phase epitaxy. Appl. Phys. Lett. 98, 233107.

Bulgarini, G., Reimer, M.E., Hocevar, M., Bakkers, E.P.A.M., Kouwenhoven, L.P., Zwiller, V., 2012. Avalanche amplification of a single exciton in a semiconductor nanowire. Nat. Photonics 6, 455–458.

Calarco, R., Marso, M., Richter, T., Aykanat, A.I., Meijers, R., Hart, A.V., Stoica, T., Luth, H., 2005. Size-dependent photoconductivity in MBE-grown GaN-nanowires. Nano Lett. 5, 981–984.

Cavallini, A., Polenta, L., Rossi, M., Stoica, T., Calarco, R., Meijers, R.J., Richter, T., Lüth, H., 2007. Franz-Keldysh effect in GaN nanowires. Nano Lett. 7, 2166–2170.

Chen, R.-S., Chen, H.-Y., Lu, C.-Y., Chen, K.-H., Chen, C.-P., Chen, L.-C., Yang, Y.-J., 2007. Ultrahigh photocurrent gain in m-axial GaN nanowires. Appl. Phys. Lett. 91, 223106.

Chen, H.-Y., Chen, R.-S., Rajan, N.K., Chang, F.-C., Chen, L.-C., Chen, K.-H., Yang, Y.-J., Reed, M.A., 2011. Size-dependent persistent photocurrent and surface band bending in m-axial GaN nanowires. Phys. Rev. B 84, 205443.

Cheng, K., Cheng, G., Wang, S.J., Li, L.S., Dai, S.X., Zhang, X.T., Zou, B.S., Du, Z.L., 2007. Surface states dominative Au Schottky contact on vertical aligned ZnO nanorod arrays synthesized by low-temperature growth. New J. Phys. 9, 214.

Cheng, G., Li, Z., Wang, S., Gong, H., Cheng, K., Jiang, X., Zhou, S., Du, Z., Cui, T., Zou, G., 2008. The unsaturated photocurrent controlled by two-dimensional barrier geometry of a single ZnO nanowire Schottky photodiode. Appl. Phys. Lett. 93, 123103.

Chuang, L.C., Sedgwick, F.G., Chen, R., Ko, W.S., Moewe, M., Ng, K.W., Tran, T.T., Chang-Hasnain, C., 2011. GaAs-based nanoneedle light emitting diode and avalanche photodiode monolithically integrated on a silicon substrate. Nano Lett. 11, 385–390.

Couteau, C., Larrue, A., Wilhelm, C., Soci, C., 2015. Nanowire lasers. Nanophotonics 4, 90–107.

Czaban, J.A., Thompson, D.A., Lapierre, R.R., 2009. GaAs core-shell nanowires for photovoltaic applications. Nano Lett. 9, 148–154.

Dai, X., Zhang, S., Wang, Z., Adamo, G., Liu, H., Huang, Y., Couteau, C., Soci, C., 2014. GaAs/AlGaAs nanowire photodetector. Nano Lett. 14, 2688–2693.

De Vlaminck, I., Van Dorpe, P., Lagae, L., Borghs, G., 2007. Local electrical detection of single nanoparticle plasmon resonance. Nano Lett. 7, 703–706.

Deng, K., Li, L., 2014. CdS nanoscale photodetectors. Adv. Mater. 26, 2619–2635.

Desiatov, B., Goykhman, I., Mazurski, N., Shappir, J., Khurgin, J.B., Levy, U., 2015. Plasmonic enhanced silicon pyramids for internal photoemission Schottky detectors in the near-infrared regime. Optica 2, 335.
Doh, Y.-J., Maher, K.N., Ouyang, L., Yu, C.L., Park, H., Park, J., 2008. Electrically driven light emission from individual CdSe nanowires. Nano Lett. 8, 4552–4556.
Driggers, R.G., 2003. Encyclopedia of Optical Engineering. Marcel Dekker, New York.
Dufaux, T., Burghard, M., Kern, K., 2012. Efficient charge extraction out of nanoscale Schottky contacts to CdS nanowires. Nano Lett. 12, 2705–2709.
Erhard, N., Seifert, P., Prechtel, L., Hertenberger, S., Karl, H., Abstreiter, G., Koblmüller, G., Holleitner, A.W., 2013. Ultrafast photocurrents and THz generation in single InAs-nanowires. Ann. Phys. 525, 180–188.
Erhard, N., Sarwar, A.T., Yang, F., Mccomb, D.W., Myers, R.C., Holleitner, A.W., 2015. Optical control of internal electric fields in band gap-graded InGaN nanowires. Nano Lett. 15, 332–338.
Falk, A.L., Koppens, F.H.L., Yu, C.L., Kang, K., De Leon Snapp, N., Akimov, A.V., Jo, M.-H., Lukin, M.D., Park, H., 2009. Near-field electrical detection of optical plasmons and single-plasmon sources. Nat. Phys. 5, 475–479.
Fan, Z.Y., Chang, P.C., Lu, J.G., Walter, E.C., Penner, R.M., Lin, C.H., Lee, H.P., 2004. Photoluminescence and polarized photodetection of single ZnO nanowires. Appl. Phys. Lett. 85, 6128–6130.
Gallo, E.M., Chen, G., Currie, M., Mcguckin, T., Prete, P., Lovergine, N., Nabet, B., Spanier, J.E., 2011. Picosecond response times in GaAs/AlGaAs core/shell nanowire-based photodetectors. Appl. Phys. Lett. 98, 241113.
Garnett, E., Yang, P., 2010. Light trapping in silicon nanowire solar cells. Nano Lett. 10, 1082–1087.
Garrido, J.A., Monroy, E., Izpura, I., Muñoz, E., 1998. Photoconductive gain modelling of GaN photodetectors. Semicond. Sci. Technol. 13, 563.
Ghosh, R., Basak, D., 2007. Electrical and ultraviolet photoresponse properties of quasialigned ZnO nanowires/p-Si heterojunction. Appl. Phys. Lett. 90, 243106.
Gonzalez-Posada, F., Songmuang, R., Den Hertog, M., Monroy, E., 2012. Room-temperature photodetection dynamics of single GaN nanowires. Nano Lett. 12, 172–176.
GonzáLez-Posada, F., Songmuang, R., Den Hertog, M., Monroy, E., 2013. Environmental sensitivity of n-i-n and undoped single GaN nanowire photodetectors. Appl. Phys. Lett. 102, 213113.
Gu, Y., Kwak, E.-S., Lensch, J.L., Allen, J.E., Odom, T.W., Lauhon, L.J., 2005. Near-field scanning photocurrent microscopy of a nanowire photodetector. Appl. Phys. Lett. 87, 043111.
Gu, Y., Romankiewicz, J.P., David, J.K., Lensch, J.L., Lauhon, L.J., Kwak, E.S., Odom, T.W., 2006. Local photocurrent mapping as a probe of contact effects and charge carrier transport in semiconductor nanowire devices. J. Vac. Sci. Technol. B 24, 2172–2177.
Guo, N., Hu, W., Liao, L., Yip, S., Ho, J.C., Miao, J., Zhang, Z., Zou, J., Jiang, T., Wu, S., Chen, X., Lu, W., 2014. Anomalous and highly efficient InAs nanowire phototransistors based on majority carrier transport at room temperature. Adv. Mater. 26, 8203–8209.
Gutsche, C., Lysov, A., Braam, D., Regolin, I., Keller, G., Li, Z.-A., Geller, M., Spasova, M., Prost, W., Tegude, F.-J., 2012. n-GaAs/InGaP/p-GaAs core-multishell nanowire diodes for efficient light-to-current conversion. Adv. Funct. Mater. 22, 929–936.
Han, S., Jin, W., Zhang, D.H., Tang, T., Li, C., Liu, X.L., Liu, Z.Q., Lei, B., Zhou, C.W., 2004. Photoconduction studies on GaN nanowire transistors under UV and polarized UV illumination. Chem. Phys. Lett. 389, 176–180.

Han, N., Wang, F., Yip, S., Hou, J.J., Xiu, F., Shi, X., Hui, A.T., Hung, T., Ho, J.C., 2012. GaAs nanowire Schottky barrier photovoltaics utilizing Au–Ga alloy catalytic tips. Appl. Phys. Lett. 101, 013105.
Harnack, O., Pacholski, C., Weller, H., Yasuda, A., Wessels, J.M., 2003. Rectifying behavior of electrically aligned ZnO nanorods. Nano Lett. 3, 1097–1101.
Hayden, O., Agarwal, R., Lieber, C.M., 2006. Nanoscale avalanche photodiodes for highly sensitive and spatially resolved photon detection. Nat. Mater. 5, 352–356.
Heo, Y.W., Tien, L.C., Kwon, Y., Norton, D.P., Pearton, S.J., Kang, B.S., Ren, F., 2004a. Depletion-mode ZnO nanowire field-effect transistor. Appl. Phys. Lett. 85, 2274–2276.
Heo, Y.W., Tien, L.C., Norton, D.P., Pearton, S.J., Kang, B.S., Ren, F., Laroche, J.R., 2004b. Pt/ZnO nanowire Schottky diodes. Appl. Phys. Lett. 85, 3107–3109.
Holm, J.V., Jorgensen, H.I., Krogstrup, P., Nygard, J., Liu, H., Aagesen, M., 2013. Surface-passivated GaAsP single-nanowire solar cells exceeding 10% efficiency grown on silicon. Nat. Commun. 4, 1498.
Hu, L., Chen, G., 2007. Analysis of optical absorption in silicon nanowire arrays for photovoltaic applications. Nano Lett. 7, 3249–3252.
Hu, S., Chi, C.-Y., Fountaine, K.T., Yao, M., Atwater, H.A., Dapkus, P.D., Lewis, N.S., Zhou, C., 2013. Optical, electrical, and solar energy-conversion properties of gallium arsenide nanowire-array photoanodes. Energy Environ. Sci. 6, 1879.
Jacopin, G., De Luna Bugallo, A., Rigutti, L., Lavenus, P., Julien, F.H., Lin, Y.-T., Tu, L.-W., Tchernycheva, M., 2014. Interplay of the photovoltaic and photoconductive operation modes in visible-blind photodetectors based on axial p-i-n junction GaN nanowires. Appl. Phys. Lett. 104, 023116.
Jain, V., Nowzari, A., Wallentin, J., Borgström, M.T., Messing, M.E., Asoli, D., Graczyk, M., Witzigmann, B., Capasso, F., Samuelson, L., Pettersson, H., 2015. Study of photocurrent generation in InP nanowire-based p+-i-n + photodetectors. Nano Res. 7, 544–552.
Jiang, N., Gao, Q., Parkinson, P., Wong-Leung, J., Mokkapati, S., Breuer, S., Tan, H.H., Zheng, C.L., Etheridge, J., Jagadish, C., 2013. Enhanced minority carrier lifetimes in GaAs/AlGaAs core–shell nanowires through shell growth optimization. Nano Lett. 13, 5135–5140.
Jie, J.S., Zhang, W.J., Jiang, Y., Meng, X.M., Li, Y.Q., Lee, S.T., 2006. Photoconductive characteristics of single-crystal CdS nanoribbons. Nano Lett. 6, 1887–1892.
Kayes, B.M., Atwater, H.A., Lewis, N.S., 2005. Comparison of the device physics principles of planar and radial p-n junction nanorod solar cells. J. Appl. Phys. 97, 114302.
Kim, D.C., Dheeraj, D.L., Fimland, B.O., Weman, H., 2013. Polarization dependent photocurrent spectroscopy of single wurtzite GaAs/AlGaAs core-shell nanowires. Appl. Phys. Lett. 102, 142107.
Krogstrup, P., Jorgensen, H.I., Heiss, M., Demichel, O., Holm, J.V., Aagesen, M., Nygard, J., Fontcuberta, I., Morral, A., 2013. Single-nanowire solar cells beyond the Shockley-Queisser limit. Nat. Photonics 7, 306–310.
Kuo, C.-H., Wu, J.-M., Lin, S.-J., Chang, W.-C., 2013. High sensitivity of middle-wavelength infrared photodetectors based on an individual InSb nanowire. Nanoscale Res. Lett. 8, 327.
Li, Q.H., Liang, Y.X., Wan, Q., Wang, T.H., 2004. Oxygen sensing characteristics of individual ZnO nanowire transistors. Appl. Phys. Lett. 85, 6389–6391.
Liu, Z., Luo, T., Liang, B., Chen, G., Yu, G., Xie, X., Chen, D., Shen, G., 2013. High-detectivity InAs nanowire photodetectors with spectral response from ultraviolet to near-infrared. Nano Res. 6, 775–783.
Logeeswaran, V.J., Sarkar, A., Islam, M.S., Kobayashi, N.P., Straznicky, J., Li, X., Wu, W., Mathai, S., Tan, M.R.T., Wang, S.Y., Williams, R.S., 2008. A 14-ps full width at half

maximum high-speed photoconductor fabricated with intersecting InP nanowires on an amorphous surface. Appl. Phys. Mater. Sci. Process. 91, 1–5.
Luo, L., Zhang, Y.F., Mao, S.S., Lin, L.W., 2006. Fabrication and characterization of ZnO nanowires based UV photodiodes. Sens. Actuators A Phys. 127, 201–206.
Luo, L.B., Zeng, L.H., Xie, C., Yu, Y.Q., Liang, F.X., Wu, C.Y., Wang, L., Hu, J.G., 2014. Light trapping and surface plasmon enhanced high-performance NIR photodetector. Sci. Report. 4, 3914.
Martien Den, H., Rudeesun, S., Fernando, G.-P., Eva, M., 2013. Single GaN-based nanowires for photodetection and sensing applications. Jpn. J. Appl. Phys. 52. 11NG01.
Miao, J., Hu, W., Guo, N., Lu, Z., Zou, X., Liao, L., Shi, S., Chen, P., Fan, Z., Ho, J.C., Li, T.-X., Chen, X.S., Lu, W., 2014. Single InAs nanowire room-temperature near-infrared photodetectors. ACS Nano 8, 3628–3635.
Milnes, A.G., Feucht, D.L., 1972. Heterojunctions and Metal-Semiconductor Junctions. Academic Press, New York.
Monroy, E., Omnès, F., Calle, F., 2003. Wide-bandgap semiconductor ultraviolet photodetectors. Semicond. Sci. Technol. 18, R33–R51.
Muskens, O.L., Borgstrom, M.T., Bakkers, E.P.A.M., Rivas, J.G., 2006. Giant optical birefringence in ensembles of semiconductor nanowires. Appl. Phys. Lett. 89, 233117.
Muskens, O.L., Rivas, J.G.M., Algra, R.E., Bakkers, E.P.A.M., Lagendijk, A., 2008. Design of light scattering in nanowire materials for photovoltaic applications. Nano Lett. 8, 2638–2642.
Nabet, B., Cola, A., Cataldo, A., Chen, X., Quaranta, F., 2003. Photodetectors based on heterostructures for opto-electronic applications. IEEE Trans. Microwave Theory Tech. 51, 2063–2072.
Peng, G., Zhou, Y., He, Y., Yu, X., Zhang, X.A., Li, G.Y., Haick, H., 2015. UV-induced SiC nanowire sensors. J. Phys. D Appl. Phys. 48, 055102.
Persano, A., Nabet, B., Taurino, A., Prete, P., Lovergine, N., Cola, A., 2011. Polarization anisotropy of individual core/shell GaAs/AlGaAs nanowires by photocurrent spectroscopy. Appl. Phys. Lett. 98, 153106.
Peter, C.S., Kerry, J.V., 1990. Analytical technique for determining the polarization dependence of optical matrix elements in quantum wires with band-coupling effects. Appl. Phys. Lett. 57, 545–547.
Pettersson, H., Trägårdh, J., Persson, A.I., Landin, L., Hessman, D., Samuelson, L., 2006. Infrared photodetectors in heterostructure nanowires. Nano Lett. 6, 229–232.
Pettersson, H., Zubritskaya, I., Nghia, N.T., Wallentin, J., Borgstrom, M.T., Storm, K., Landin, L., Wickert, P., Capasso, F., Samuelson, L., 2012. Electrical and optical properties of InP nanowire ensemble p(+)-i-n(+) photodetectors. Nanotechnology 23, 135201.
Polenta, L., Rossi, M., Cavallini, A., Calarco, R., Marso, M., Meijers, R., Richter, T., Stoica, T., Lüth, H., 2008. Investigation on localized states in GaN nanowires. ACS Nano 2, 287–292.
Prades, J.D., Hernandez-Ramirez, F., Jimenez-Diaz, R., Manzanares, M., Andreu, T., Cirera, A., Romano-Rodriguez, A., Morante, J.R., 2008a. The effects of electron-hole separation on the photoconductivity of individual metal oxide nanowires. Nanotechnology 19, 465501.
Prades, J.D., Jimenez-Diaz, R., Hernandez-Ramirez, F., Fernandez-Romero, L., Andreu, T., Cirera, A., Romano-Rodriguez, A., Cornet, A., Morante, J.R., Barth, S., Mathur, S., 2008b. Toward a systematic understanding of photodetectors based on individual metal oxide nanowires. J. Phys. Chem. C 112, 14639–14644.
Prechtel, L., Padilla, M., Erhard, N., Karl, H., Abstreiter, G., Fontcuberta, I.M.A., Holleitner, A.W., 2012. Time-resolved photoinduced thermoelectric and transport currents in GaAs nanowires. Nano Lett. 12, 2337–2341.

Qi, J., Belcher, A.M., White, J.M., 2003. Spectroscopy of individual silicon nanowires. Appl. Phys. Lett. 82, 2616–2618.
Reimer, M.E., 2011. Single photon emission and detection at the nanoscale utilizing semiconductor nanowires. J. Nanophotonics 5, 053502.
Reui-San, C., Hsin-Yi, C., Chien-Yao, L., Kuei-Hsien, C., Chin-Pei, C., Li-Chyong, C., Ying-Jay, Y., 2007. Ultrahigh photocurrent gain in m-axial GaN nanowires. Appl. Phys. Lett. 91, 223106.
Rigutti, L., Jacopin, G., Bugallo Ade, L., Tchernycheva, M., Warde, E., Julien, F.H., Songmuang, R., Galopin, E., Largeau, L., Harmand, J.C., 2010a. Investigation of the electronic transport in GaN nanowires containing GaN/AlN quantum discs. Nanotechnology 21, 425206.
Rigutti, L., Tchernycheva, M., De Luna Bugallo, A., Jacopin, G., Julien, F.H., Zagonel, L.F., March, K., Stephan, O., Kociak, M., Songmuang, R., 2010b. Ultraviolet photodetector based on GaN/AlN quantum disks in a single nanowire. Nano Lett. 10, 2939–2943.
Ruda, H.E., Shik, A., 2005. Polarization-sensitive optical phenomena in semiconducting and metallic nanowires. Phys. Rev. B 72, 115308.
Ruda, H.E., Shik, A., 2006. Polarization-sensitive optical phenomena in thick semiconducting nanowires. J. Appl. Phys. 100, 024314.
Sanford, N.A., Blanchard, P.T., Bertness, K.A., Mansfield, L., Schlager, J.B., Sanders, A.W., Roshko, A., Burton, B.B., George, S.M., 2010. Steady-state and transient photoconductivity in c-axis GaN nanowires grown by nitrogen-plasma-assisted molecular beam epitaxy. J. Appl. Phys. 107, 034318.
Sanford, N.A., Robins, L.H., Blanchard, P.T., Soria, K., Klein, B., Eller, B.S., Bertness, K.A., Schlager, J.B., Sanders, A.W., 2013. Studies of photoconductivity and field effect transistor behavior in examining drift mobility, surface depletion, and transient effects in Si-doped GaN nanowires in vacuum and air. J. Appl. Phys. 113, 174306.
Senanayake, P., Hung, C.H., Shapiro, J., Lin, A., Liang, B., Williams, B.S., Huffaker, D.L., 2011. Surface plasmon-enhanced nanopillar photodetectors. Nano Lett. 11, 5279–5283.
Senanayake, P., Hung, C.H., Farrell, A., Ramirez, D.A., Shapiro, J., Li, C.K., Wu, Y.R., Hayat, M.M., Huffaker, D.L., 2012. Thin 3D multiplication regions in plasmonically enhanced nanopillar avalanche detectors. Nano Lett. 12, 6448–6452.
Shin, J.C., Lee, A., Katal Mohseni, P., Kim, D.Y., Yu, L., Kim, J.H., Kim, H.J., Choi, W.J., Wasserman, D., Choi, K.J., Li, X., 2013. Wafer-Scale production of uniform InAsyP1–y nanowire array on silicon for heterogeneous integration. ACS Nano 7, 5463–5471.
Soci, C., Zhang, A., Xiang, B., Dayeh, S.A., Aplin, D.P.R., Park, J., Bao, X.Y., Lo, Y.H., Wang, D., 2007. ZnO nanowire UV photodetectors with high internal gain. Nano Lett. 7, 1003–1009.
Soci, C., Zhang, A., Bao, X.-Y., Kim, H., Lo, Y., Wang, D., 2010. Nanowire photodetectors. J. Nanosci. Nanotechnol. 10, 1430–1449.
Son, M.S., Im, S.I., Park, Y.S., Park, C.M., Kang, T.W., Yoo, K.H., 2006. Ultraviolet photodetector based on single GaN nanorod p-n junctions. Mater. Sci. Eng. C Biomim. Supramol. Syst. 26, 886–888.
Sze, S.M., 1981. Physics of Semiconductor Devices. Wiley, New York.
Tchernycheva, M., Rigutti, L., Jacopin, G., Bugallo, A.D.L., Lavenus, P., Julien, F.H., Timofeeva, M., Bouravleuv, A.D., Cirlin, G.E., Dhaka, V., Lipsanen, H., Largeau, L., 2012. Photovoltaic properties of GaAsP core–shell nanowires on Si(001) substrate. Nanotechnology 23, 265402.
Tchernycheva, M., Messanvi, A., De Luna Bugallo, A., Jacopin, G., Lavenus, P., Rigutti, L., Zhang, H., Halioua, Y., Julien, F.H., Eymery, J., Durand, C., 2014. Integrated photonic platform based on InGaN/GaN nanowire emitters and detectors. Nano Lett. 14, 3515–3520.

Van Kouwen, M.P., Van Weert, M.H.M., Reimer, M.E., Akopian, N., Perinetti, U., Algra, R.E., Bakkers, E.P.A.M., Kouwenhoven, L.P., Zwiller, V., 2010. Single quantum dot nanowire photodetectors. Appl. Phys. Lett. 97, 113108.
Wallentin, J., Anttu, N., Asoli, D., Huffman, M., Åberg, I., Magnusson, M.H., Siefer, G., Fuss-Kailuweit, P., Dimroth, F., Witzigmann, B., Xu, H.Q., Samuelson, L., Deppert, K., Borgström, M.T., 2013. InP nanowire array solar cells achieving 13.8% efficiency by exceeding the Ray optics limit. Science 339, 1057–1060.
Wang, L., Asbeck, P., 2006. Analysis of photoelectronic response in semiconductor nanowires. In: Sixth IEEE Conference on Nanotechnology, 2006, IEEE-NANO 2006, vol. 2, pp. 716–719.
Wang, J.F., Gudiksen, M.S., Duan, X.F., Cui, Y., Lieber, C.M., 2001. Highly polarized photoluminescence and photodetection from single indium phosphide nanowires. Science 293, 1455–1457.
Wang, K., Chen, J.J., Zhou, W.L., Zhang, Y., Yan, Y.F., Pern, J., Mascarenhas, A., 2008. Direct growth of highly mismatched type II ZnO/ZnSe core/shell nanowire arrays on transparent conducting oxide substrates for solar cell applications. Adv. Mater. 20, 3248.
Wang, X., Zhang, Y., Chen, X., He, M., Liu, C., Yin, Y., Zou, X., Li, S., 2014. Ultrafast, superhigh gain visible-blind UV detector and optical logic gates based on nonpolar a-axial GaN nanowire. Nanoscale 6, 12009–12017.
Wei, W., Bao, X.-Y., Soci, C., Ding, Y., Wang, Z.-L., Wang, D., 2009. Direct heteroepitaxy of vertical InAs nanowires on Si substrates for broad band photovoltaics and photodetection. Nano Lett. 9, 2926–2934.
Wei, T.-Y., Huang, C.-T., Hansen, B.J., Lin, Y.-F., Chen, L.-J., Lu, S.-Y., Wang, Z.L., 2010. Large enhancement in photon detection sensitivity via Schottky-gated CdS nanowire nanosensors. Appl. Phys. Lett. 96, 013508.
Wilhelm, C., Larrue, A., Dai, X., Migas, D., Soci, C., 2012. Anisotropic photonic properties of III-V nanowires in the zinc-blende and wurtzite phase. Nanoscale 4, 1446–1454.
Wu, H., Sun, Y., Lin, D., Zhang, R., Zhang, C., Pan, W., 2009. GaN nanofibers based on electrospinning: facile synthesis, controlled assembly, precise doping, and application as high performance UV photodetector. Adv. Mater. 21, 227–231.
Wu, P., Dai, Y., Sun, T., Ye, Y., Meng, H., Fang, X., Yu, B., Dai, L., 2011. Impurity-dependent photoresponse properties in single CdSe nanobelt photodetectors. ACS Appl. Mater. Interfaces 3, 1859–1864.
Xia, H., Lu, Z.-Y., Li, T.-X., Parkinson, P., Liao, Z.-M., Liu, F.-H., Lu, W., Hu, W.-D., Chen, P.-P., Xu, H.-Y., Zou, J., Jagadish, C., 2012. Distinct photocurrent response of individual GaAs nanowires induced by n-type doping. ACS Nano 6, 6005–6013.
Xie, X., Kwok, S.Y., Lu, Z., Liu, Y., Cao, Y., Luo, L., Zapien, J.A., Bello, I., Lee, C.S., Lee, S.T., Zhang, W., 2012. Visible-NIR photodetectors based on CdTe nanoribbons. Nanoscale 4, 2914–2919.
Xinyuan, Z., Wei, C.M., Yang, L., Chou, M.Y., 2004. Quantum confinement and electronic properties of silicon nanowires. Phys. Rev. Lett. 92, 236805.
Yang, C., Barrelet, C.J., Capasso, F., Lieber, C.M., 2006. Single p-type/intrinsic/n-type silicon nanowires as nanoscale avalanche photodetectors. Nano Lett. 6, 2929–2934.
Ye, Y., Dai, L., Wen, X., Wu, P., Pen, R., Qin, G., 2010. High-performance single CdS nanobelt metal-semiconductor field-effect transistor-based photodetectors. ACS Appl. Mater. Interfaces 2, 2724–2727.
Zhang, D., Li, C., Han, S., Liu, X., Tang, T., Jin, W., Zhou, C., 2003. Ultraviolet photodetection properties of indium oxide nanowires. Appl. Phys. A Mater. Sci. Process. 77, 163–166.
Zhang, Z.H., Qi, X.Y., Han, J.K., Duan, X.F., 2006a. Investigation on optical properties of ZnO nanowires by electron energy-loss spectroscopy. Micron 37, 229–233.

Zhang, Z.Y., Jin, C.H., Liang, X.L., Chen, Q., Peng, L.M., 2006b. Current-voltage characteristics and parameter retrieval of semiconducting nanowires. Appl. Phys. Lett. 88, 073102.

Zhang, Y., Wang, L.-W., Mascarenhas, A., 2007. "Quantum coaxial cables" for solar energy harvesting. Nano Lett. 7, 1264–1269.

Zhang, H., Babichev, A.V., Jacopin, G., Lavenus, P., Julien, F.H., Egorov, A.Yu., Zhang, J., Pauporté, T., Tchernycheva, M., 2013. Characterization and modeling of a ZnO nanowire ultraviolet photodetector with graphene transparent contact. J. Appl. Phys. 114, 234505.

Zhen, G., Dongxu, Z., Yichun, L., Dezhen, S., Jiying, Z., Binghui, L., 2008. Visible and ultraviolet light alternative photodetector based on ZnO nanowire/n-Si heterojunction. Appl. Phys. Lett. 93, 163501.